

$J = 1 - 0$ HCN toward bright far-infrared sources in the outer Galaxy

L. Pirogov

Institute of Applied Physics of the Russian Academy of Sciences, Uljanov st. 46, 603600 Nizhny Novgorod, Russia

Received 2 February 1999 / Accepted 3 June 1999

Abstract. Results of the $J = 1 - 0$ HCN observations toward 34 bright far-infrared sources selected from the IRAS Point Source Catalog are reported. Together with 17 sources observed in this line earlier (Pirogov et al., 1996) they form a complete sample of the sources with flux densities $S(100\ \mu\text{m}) > 500$ Jy and $\delta > 0^\circ$ in the outer Galaxy.

The HCN data are compared with the HCO^+ , NH_3 , CS and CO data taken from literature. Prominent correlations with nearly similar slopes of ~ 1 are revealed between line integrated intensities of the molecules known to be high density tracers (HCN, HCO^+ , NH_3 and CS). The correlations become higher after adding the data for dark clouds, small globules and cirrus cores implying similar excitation and formation mechanisms of the considered molecules. Collisional excitation in regions with different densities as well as different molecular abundances and velocity dispersions in different types of cores seem to be important in producing these correlations. The following relations hold on the average over ~ 3 orders of magnitude of integrated intensities: $I(\text{HCN}) \gtrsim I(\text{HCO}^+) \sim I(\text{CS}) > I(\text{NH}_3)$ where ammonia integrated intensities are several times lower than HCN ones. Correlations are also found between HCN and CO integrated intensities for the sample sources as well as between HCN line widths and those of other species. The HCN lines have the same widths as the HCO^+ ones and are larger than CS and especially NH_3 line widths.

Weak correlations are found between HCN line widths and luminosities of IRAS sources as well as between HCN integrated intensities, IRAS flux densities at $100\ \mu\text{m}$ and luminosities of IRAS sources divided by distance squared.

The sources with most intense HCN lines have associated water masers and molecular outflows while the lack of associated maser and outflow implies weak or no HCN emission.

In order to reproduce the anomalies of the $J = 1 - 0$ HCN hyperfine structure ($R_{12} < 0.6$) detected in several sources together with suprathreshold line widths the model calculations are performed. Two models have been considered: a microturbulent one with a smooth density distribution and a clumpy model. It is found that in the parameter space explored a clumpy model is preferable in comparison with a microturbulent one due to the absence of self-reversals on calculated profiles and the possibility of reproducing HCN profile anomalies and suprathreshold line widths.

Detailed clumpy model simulations have been performed to fit the observed HCN and H^{13}CN spectra toward S140 IRS1. The best fit model parameters are calculated, including radial dependencies of clump density and volume filling factor.

Key words: stars: formation – ISM: clouds – ISM: molecules – radio lines: ISM – ISM: individual objects: S 140

1. Introduction

Very young massive stars at early stages of evolution are often associated with bright infrared sources, ultracompact H II regions, embedded in dense molecular cloud cores. Observations in molecular lines that trace high-density gas can give important information about physical conditions within dense cores as well as about the relationship between young stellar objects and their parent clouds cores. Usually, investigations are concentrated on distinct objects observed in various molecular lines which are indicators of particular physical parameters within cores (e.g. density, temperature) also taking into account available infrared, radio and optical data. Another direction of research concentrates on observations of samples of objects chosen according to particular criteria in one or several molecular lines. These observations even being performed without mapping of each object give an opportunity to reveal statistical properties of a sample under study as well as to select objects for further detailed investigation.

For many years most systematic molecular line studies of star forming regions were concentrated on dense cores in dark clouds and globules which are the sites of low-mass star formation and have relatively compact and simple structure. Recently high-mass star forming regions have begun to be explored systematically (e.g. Anglada et al. 1996, Bronfman et al. 1996, Plume et al. 1992, 1997, Zinchenko et al. 1995, 1998). Criteria that a young high-mass star exists inside a dense core are the existence of a high luminosity infrared point source satisfying the color criteria of Wood & Churchwell (1989) or ultracompact H II region observed in radio wavelength continuum. Water masers as well as high-velocity molecular outflows which are indications of dynamic activity are often associated with high-mass stars at an early stage of evolution.

The HCN molecule is known to be a widely spread high-density tracer of molecular clouds, star forming regions, envelopes of late-type stars and other galaxies. An early $J = 1 - 0$ HCN survey toward molecular clouds associated with galactic optical H II regions and enhanced CO emission (Burov et al. 1988) detected HCN emission in more than half of the objects observed, although there were sensitivity, spectral resolution and, probably, pointing accuracy limitations during these observations. The present paper includes the results of new $J = 1 - 0$ HCN observations toward 34 bright FIR sources with flux densities $S(100 \mu\text{m}) > 500$ Jy according to the IRAS Point Source Catalog (PSC) (IRAS Catalogs 1988) located in the outer Galaxy in the $0^h - 12^h$ right ascension range with $\delta > 0^\circ$. Together with 17 sources previously observed in this line (Pirogov et al. 1996, hereafter Paper I) these objects form a complete sample of bright IRAS point sources in the given coordinate range. Most of them can be associated with high-mass stars embedded in dense cores according to their $60 \mu\text{m}/12 \mu\text{m}$ and $25 \mu\text{m}/12 \mu\text{m}$ colors (Wood & Churchwell, 1989).

The goal of this investigation is two-fold. The first one is to study physical properties of dense cores associated with bright FIR sources by comparing the HCN data with other available molecular line data as well as with parameters of IRAS sources. Most of the sample sources were observed earlier in the $J = 1 - 0$ CO line by Snell et al. (1988, 1990) from which we took the sampling criteria. All the sample sources were also observed by Schreyer et al. (1996) in the $J = 1 - 0$ HCO⁺ and NH₃ (1,1) and (2,2) lines. The sample sources were partly observed in the $J = 2 - 1$ CS line by Carpenter et al. (1993), Bronfman et al. (1996) and Zinchenko et al. (1998). All these data sets are obtained with nearly the same spatial resolution ($\sim 40'' - 60''$) and give an opportunity to compare different line parameters with each other.

Our second goal is to select the most adequate model of HCN emission. The hyperfine structure of the HCN $J = 1 - 0$ transition which is clearly resolved in many sources of the sample gives invaluable additional information about dense gas conditions although they complicate the picture due to non-LTE ratios. Two models, a microturbulent one with a smooth density distribution and a clumpy model have been used to reproduce the observed HCN line profiles. It is shown that the problem of non-LTE $J = 1 - 0$ HCN hfs ratios together with suprathreshold line widths can be most easily understood only within a clumpy model. We performed detailed HCN and H¹³CN clumpy model simulations for the dense core associated with the bright infrared source S140 IRS1 and obtained a good agreement between model and observed spectra.

2. Observations

The $J = 1 - 0$ HCN observations (at 88631.8 MHz) were performed in February 1996 at the 20-m radiotelescope of the Onsala Space Observatory (OSO)¹. The telescope was equipped

¹ The OSO 20-m telescope is operated by the Swedish National Facility for Radio Astronomy, Onsala Space Observatory at Chalmers University of Technology

with an SIS mixer. The system noise temperature (SSB) varied between 300 K and 500 K during observations depending on elevation and weather conditions. We used the backend filterbank spectrometer with 250 KHz frequency resolution corresponding to $\sim 0.83 \text{ km s}^{-1}$ velocity resolution at the $J = 1 - 0$ HCN frequency. The telescope has $45''$ beam width at the HCN frequency that corresponds to spatial resolutions 0.1–1.8 pc for our sources. The pointing accuracy was checked regularly by observations of SiO masers and did not exceed $\sim 10''$ but usually was as good as $\leq 5''$. The observations were performed in the dual beam-switching mode with the offset position $\sim 11'$ in azimuth. We express line intensities in the units of main beam brightness temperature (T_{MB}), which is an antenna temperature corrected for main beam efficiency, radome and atmospheric attenuation. The main beam efficiency was taken to be 0.59 at the HCN $J = 1 - 0$ frequency (L.E.B. Johansson, private communication).

The source list is given in Table 1. Apart from the sources observed at OSO this list also contains the sources previously observed at the RT-22 CrAO radiotelescope (Paper I). Both these subsamples form a complete sample of bright FIR sources in the outer Galaxy ($\alpha = 0^h - 12^h$) having $S(100 \mu\text{m}) > 500$ Jy and $\delta > 0^\circ$. Each of the sources were observed with a single pointing centered on the position of IRAS point source (IRAS Catalogs 1988).

Table 1 contains coordinates and distances to the objects as well as the names of associated objects. Most of the distances which are the distances to OB associations and H II regions that are associated in position and velocity with FIR sources are taken from Snell et al. (1988, 1990) and Lada (1985). For two sources (03211+5446 and 04073+5102) the kinematic distances are given. Corresponding references are summarized in the footnotes of the table.

3. Observational results and LTE column densities

The results of data processing are compiled in Table 2. For most of the sources the results of Gaussian fitting of the HCN triplet with fixed separation between components of the same width corresponding to the $J = 1 - 0$ HCN hyperfine structure are given. Table 2 includes the peak main beam temperature and velocity of the $F = 2 - 1$ component, the line width (FWHM), and relative intensities of the satellite components, R_{12} and R_{02} (Columns 2-6). Total integrated intensities are given in Column 7. The HCN spectrum toward 05345+3157 has been reprocessed and the corrected results are given in Table 2 instead of those published in Paper I. Many sources demonstrate either prominent high-velocity wings (00338+6312, 00494+5617, 02219+6152, 02232+6138, 06056+2131, 06319+0415) or some additional emission features. Due to an ambiguity of deconvolving these spectra into multiple HCN triplets, we give in Table 2 the results of single triplet fitting if there are only weak additional features that do not strongly affect the main components. For those sources where fitting with a single Gaussian triplet is unsatisfactory, the peak main beam temperatures measured by eye as well as corresponding velocity and total integrated inten-

Table 1. The source list: coordinates and distances to the objects.

Name	$\alpha(1950)$ (^h) (^m) (^s)	$\delta(1950)$ ([°]) ([']) (^{''})	D (kpc)	Associated objects
00338+6312	00 33 53.3	63 12 32	0.85 ^a	RNO 1B, L1287
00494+5617	00 49 27.8	56 17 28	3.5 ^b	NGC 281, S184
01195+6136	01 19 31.7	61 36 35	2.0 ^c	S187
02219+6152	02 21 55.3	61 52 34	2.3 ^c	AFGL 326, W3-IRS5, S190
02230+6202	02 23 02.3	62 02 24	2.2 ^d	AFGL 328, W3N
02232+6138	02 23 13.7	61 38 46	2.3 ^c	AFGL 331, W3(OH)
02244+6117	02 24 27.2	61 17 47	2.2 ^e	AFGL 333, W4
02575+6017	02 57 35.6	60 17 22	2.2 ^d	AFGL 4029, IC1848, S199
02593+6016	02 59 20.6	60 16 08	2.2 ^d	AFGL 416, S201
03035+5819	03 03 33.2	58 19 21	3.0 ^f	AFGL 437, BFS 26
03064+5638	03 06 26.9	56 38 56	2.2 ^h	AFGL 5090
03211+5446	03 21 11.8	54 46 51	3.1 ^d	AFGL 5094, BFS 31
03236+5836	03 23 39.0	58 36 33	0.9 ^c	AFGL 490
03260+3111	03 26 04.7	31 11 41	0.5 ^c	NGC 1333, HH7-11
03595+5110	03 59 31.6	51 10 41	3.3 ^e	AFGL 5111, S206
04073+5102	04 07 18.5	51 02 30	8.2 ^g	AFGL 550, S209
04269+3510	04 26 57.2	35 10 01	0.8 ^c	AFGL 585, S222, LKH&101
04324+5106	04 32 28.7	51 06 39	6.0 ^d	AFGL 5124, S211
04329+5047	04 32 58.3	50 47 21	6.0 ^e	AFGL 5125, S211
05100+3723	05 10 01.7	37 23 35	2.6 ^d	AFGL 5137, S228
05197+3355	05 19 46.4	33 55 39	3.2 ^e	S230
05274+3345	05 27 27.6	33 45 37	1.8 ^d	AFGL 5142
05281+3412	05 28 07.8	34 12 46	1.8 ^d	AFGL 5144, S237
05345+3157	05 34 32.6	31 57 40	1.8 ^d	AFGL 5157
05355+3039	05 35 34.0	30 39 48	1.8 ^d	AFGL 5158
05358+3543	05 35 48.8	35 43 41	1.8 ^e	S231
05375+3540	05 37 32.1	35 40 45	1.8 ^e	S235B, BFS 46
05377+3548	05 37 46.7	35 48 25	1.8 ^e	S235
05445+0016	05 44 33.7	00 16 44	0.5 ^f	AFGL 818, NGC 2071
05480+2544	05 48 01.9	25 44 50	2.1 ^e	BFS 48
05480+2545	05 48 04.8	25 45 29	2.1 ^e	BFS 48
05490+2658	05 49 05.2	26 58 52	2.1 ^e	S242
05553+1631	05 55 20.3	16 31 46	2.0 ^h	AFGL 5173
06006+3015	06 00 41.4	30 15 05	4.7 ^e	AFGL 5176, S241
06013+3030	06 01 21.2	30 30 53	4.7 ^e	CED 061
06055+2039	06 05 33.9	20 39 47	2.0 ^b	S252A
06056+2131	06 05 40.9	21 31 32	2.0 ^h	AFGL 6366S, S247
06058+2138	06 05 53.9	21 38 57	2.0 ^h	AFGL 5180, S247
06061+2151	06 06 07.3	21 51 12	2.0 ^h	AFGL 5182, S247
06063+2040	06 06 23.0	20 40 02	2.0 ^b	AFGL 5183
06068+2030	06 06 53.0	20 30 41	2.0 ^h	AFGL 5184, S252
06073+1249	06 07 23.5	12 49 24	4.8 ^d	AFGL 5185, S270
06099+1800	06 09 57.9	18 00 12	0.8 ^c	AFGL 896, S255
06105+1756	06 10 33.0	17 56 22	2.5 ^e	S258
06114+1745	06 11 28.6	17 45 33	2.5 ^d	AFGL 5188
06117+1350	06 11 46.4	13 50 33	3.8 ^e	AFGL 902, S269
06155+2319	06 15 32.7	23 19 26	1.6 ^e	BFS 51
06308+0402	06 30 52.7	04 02 27	1.6 ^e	RNO 73
06319+0415	06 31 59.0	04 15 09	1.6 ^c	AFGL 961, GGD 18
06380+0949	06 38 00.6	09 49 24	0.8 ^e	AFGL 4519S, NGC 2264, S273
06384+0932	06 38 26.2	09 32 25	0.8 ^c	AFGL 989, NGC 2264, S273

^a Yang et al. (1991),^b Schreyer et al. (1996),^c Lada (1985),^d Snell et al. (1988),^e Snell et al. (1990),^f Henning et al. (1992),^g Brand & Blitz (1993),^h Carpenter et al. (1993).

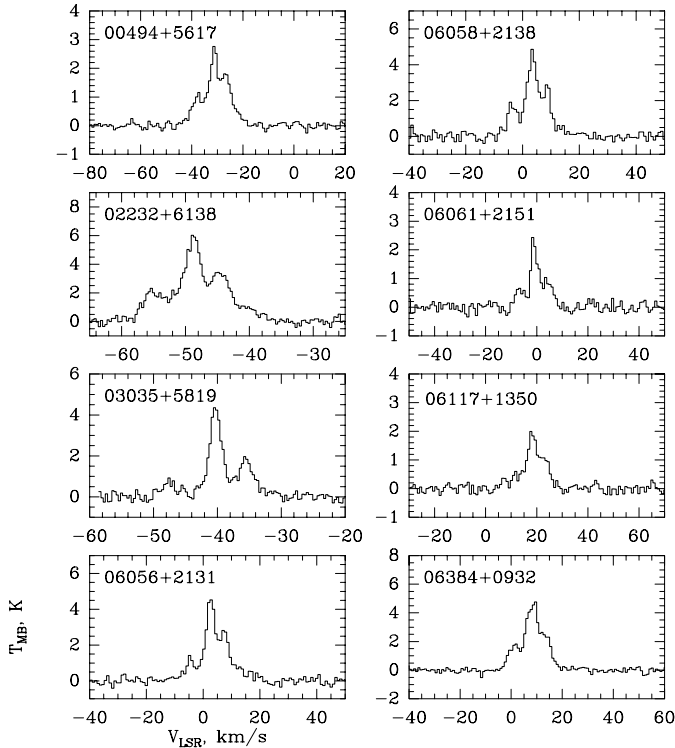


Fig. 1. The samples of the observed $J = 1 - 0$ HCN spectra

sity are given. For 04073+5102 and 06068+2030 where signal-to-noise ratios are small while the HCN spectra probably exhibit multicomponent structure, only integrated intensities for the ($-65 \text{ km s}^{-1} \dots -40 \text{ km s}^{-1}$) and ($0 \text{ km s}^{-1} \dots 30 \text{ km s}^{-1}$) velocity ranges, respectively, are given in Table 2. The HCN spectrum toward 06105+1756 contains an absorption feature which is probably due to a signal in the reference position. The integrated intensity for this source is obtained from Gaussian fitting. A few of the most intensive $J = 1 - 0$ HCN spectra are shown in Fig. 1.

HCN has been detected in 44 cases of 51, a detection rate of 86%. We did not detect any emission toward five sources of the sample while two of the sources (03595+5110 and 06380+0949) show emission features with velocities that significantly differ from CO velocities (Snell et al. 1990). For these seven sources upper limits of main beam temperatures (3σ) are given in Table 2. The upper limit for 03211+5446 from Paper I has also been corrected.

The relative intensities of the $J = 1 - 0$ HCN satellite components, $R_{12} = T_{\text{MB}}(F = 1 - 1)/T_{\text{MB}}(F = 2 - 1)$ and $R_{02} = T_{\text{MB}}(F = 0 - 1)/T_{\text{MB}}(F = 2 - 1)$, show significant variations from source to source. Note, that small signal-to-noise ratios as well as a presence of high-velocity wings or additional emission features could affect the values of R_{12} and R_{02} ratios obtained from single Gaussian fits in some cases. Among those sources that do not demonstrate any prominent additional features, several have R_{12} and R_{02} values close to the optically thin case (0.6 and 0.2, respectively) within the uncertainties of their determination. They are: 02593+6016, 04269+3510,

05345+3157, 05355+3039, 06006+3015, 06308+0402 and, probably, 06117+1350. The HCN column densities for these sources calculated under the LTE assumption ($T_{\text{ex}} = 10 \text{ K}$) using formula (2) from (Pirogov et al. 1995) lie in the range: $(3.5 - 24.4) \cdot 10^{12} \text{ cm}^{-2}$. Column density estimates only weakly depend on the assumed T_{ex} value and are close to minimum for $T_{\text{ex}} = 5 - 10 \text{ K}$. Therefore, these estimates should be treated as lower limits.

Most of the sources demonstrate prominent anomalies of hyperfine intensity ratios ($R_{12} < 0.6$, $R_{02} \gtrsim 0.2$) implying that the lines are not optically thin and not in LTE, having different excitation temperatures for the hyperfine components. In order to derive physical properties of these sources we performed non-LTE modelling with microturbulent and clumpy structures. The details of model simulations are given in Sect. 7.

4. Comparison between HCN and other molecular data

Most of the sample sources were observed earlier in the $J = 1 - 0$ CO line with the $45''$ beam width at the 14-m FCRAO radiotelescope by Snell et al. (1988, 1990). All the sample sources were observed in the NH_3 (1,1) and (2,2) lines at the 100-m Effelsberg radiotelescope ($40''$ beam width) as well as in the $J = 1 - 0$ HCO^+ line at the 14-m radiotelescope of Metsähovi Radio Station ($60''$ beam width) (Schreyer et al. 1996). 20 sources of the present sample have been mapped by Carpenter et al. (1993) in the $J = 2 - 1$ CS line at the 14-m FCRAO radiotelescope ($53''$ beam width). Also, 22 sources of the sample were included in the $J = 2 - 1$ CS survey of IRAS point sources (Bronfman et al. 1996) performed at OSO and SEST radiotelescopes with $39''$ and $50''$ beam widths, respectively; 9 sources of the sample were observed by Zinchenko et al. (1998) in the same line at the 20-m OSO radiotelescope. A comparison between $V_{\text{LSR}}(\text{HCN})$ and velocities of other molecular species shows that all of them are in excellent agreement with each other implying that molecular emission comes from the same clouds. All the data sets are obtained with nearly the same beams implying that molecular line parameters can be compared with each other.

4.1. Integrated intensity comparison

In Fig. 2(a,b) the HCO^+ and NH_3 (1,1) integrated intensities (Schreyer et al. 1996) are plotted versus those of HCN, respectively. The CS integrated intensities derived from the $J = 2 - 1$ CS data (Bronfman et al. 1996, Carpenter et al. 1993, Zinchenko et al. 1998) are given in Fig. 2(c) versus HCN. In Fig. 2(d) the CO integrated intensities for bright FIR sources (Snell et al. 1988, 1990) are plotted versus HCN. The HCO^+ , NH_3 , CO and most of the CS integrated intensities are calculated by multiplying peak line temperature and line width. The data corresponding to bright FIR sources are marked by filled squares. The intensities plotted in Fig. 2(a-c) show a higher degree of correlation (the correlation coefficients are $\sim 0.8 - 0.9$) comparing with those plotted in Fig. 2(d) (the correlation coefficient is ~ 0.6). The least-squares linear fits are shown in Fig. 2 as

Table 2. The $J = 1 - 0$ HCN observational results.

Name	$J = 1 - 0$ HCN						Telescope	H ₂ O ^a	outflow ^b
	T_{MB} (K)	V_{LSR} (km s ⁻¹)	ΔV (km s ⁻¹)	R_{12}	R_{02}	I (K km s ⁻¹)			
00338+6312	~ 5	-18.9				24.7	RT-22	Y	Y
00494+5617	~ 2.8	-31.3				26.5	OSO	Y	Y
01195+6136	<0.8						RT-22	N	N
02219+6152	~ 4	-42.8				34.2	RT-22	Y	Y
02230+6202	<0.4						OSO	N	N
02232+6138	~ 6	-48.8				46.6	RT-22	Y	Y
02244+6117	0.44(6)	-51.0	3.2(2)	0.6(1)	0.4(1)	2.2	RT-22 ^c	N	N
02575+6017	5.8(1)	-38.6	2.41(2)	0.43(2)	0.22(2)	25.6	RT-22 ^c	Y	Y
02593+6016	0.62(6)	-39.1	3.5(2)	0.7(1)	0.3(1)	4.6	OSO	Y	N
03035+5819	4.0(1)	-40.3	2.64(5)	0.45(3)	0.16(3)	19.9	RT-22	Y	Y
03064+5638	1.7(1)	-41.1	1.73(6)	0.34(5)	0.23(4)	5.0	RT-22 ^c	N	N
03211+5446	<0.6						RT-22	N	N
03236+5836	1.7(1)	-13.2	3.3(1)	0.57(6)	0.38(5)	14.2	OSO	Y	Y
03260+3111	0.70(8)	7.7	1.8(1)	0.8(1)	0.5(1)	3.8	OSO	N	N
03595+5110	<0.2						OSO	N	N
04073+5102						3.1	RT-22	N	N
04269+3510	0.54(6)	-1.7	2.2(2)	0.6(1)	0.2(1)	2.6	OSO	N	Y
04324+5106	1.7(1)	-37.3	3.0(1)	0.30(6)	0.35(6)	8.9	RT-22 ^c	N	N
04329+5047	0.28(6)	-38.3	4.0(4)	0.8(3)	0.4(2)	3.6	OSO	N	N
05100+3723	0.5(1)	-7.1	3.4(3)	0.4(1)	0.0(1)	2.1	RT-22 ^c	N	N
05197+3355	0.4(1)	-4.9	1.9(2)	0.8(3)	0.9(3)	1.6	RT-22 ^c	N	N
05274+3345	~ 3.4	-5.0				20.5	RT-22 ^c	Y	Y
05281+3412	<0.3						OSO	N	N
05345+3157	0.65(4)	-19.0	2.1(1)	0.55(7)	0.13(7)	2.1	RT-22	Y	Y
05355+3039	0.67(7)	-16.6	1.7(1)	0.6(1)	0.3(1)	2.1	RT-22 ^c	N	N
05358+3543	3.0(1)	-18.3	2.5(1)	0.35(5)	0.17(5)	11.2	RT-22 ^c	Y	Y
05375+3540	4.76(4)	-17.1	2.25(2)	0.35(1)	0.23(1)	20.5	OSO ^d	Y	Y
05377+3548	3.6(3)	-20.4	2.2(1)	0.6(1)	0.0(1)	10.8	RT-22 ^c	Y	N
05445+0016	0.5(1)	10.2	2.3(3)	0.6(2)	0.7(2)	4.5	OSO	Y	N
05480+2544	0.9(1)	-9.5	2.4(2)	0.8(2)	0.2(1)	3.7	OSO	N	N
05480+2545	2.8(1)	-9.4	3.31(7)	0.66(5)	0.35(4)	21.8	OSO	N	N
05490+2658	1.27(6)	0.6	2.8(1)	0.58(6)	0.30(5)	7.6	OSO	N	Y
05553+1631	0.51(7)	5.3	3.2(3)	0.2(1)	0.2(1)	2.5	OSO	Y	Y
06006+3015	1.45(6)	-9.1	3.5(1)	0.59(5)	0.21(4)	10.0	OSO	Y	N
06013+3030	<0.9						RT-22 ^c	N	N
06055+2039	1.1(1)	8.7	4.1(2)	0.6(1)	0.4(1)	10.9	OSO	Y	N
06056+2131	4.3(1)	2.6	3.82(6)	0.58(3)	0.24(2)	35.0	OSO	Y	Y
06058+2138	4.5(2)	3.4	4.24(8)	0.56(4)	0.41(3)	42.0	OSO	Y	Y
06061+2151	2.2(1)	-0.8	3.8(1)	0.43(5)	0.33(4)	16.7	OSO	Y	N
06063+2040	1.2(1)	8.8	2.5(1)	0.40(6)	0.16(7)	4.6	OSO	N	N
06068+2030						4.5	OSO	N	N
06073+1249	1.3(1)	25.2	2.9(1)	0.51(8)	0.36(7)	9.8	OSO	N	N
06099+1800	5.5(2)	6.8	3.9(1)	0.45(4)	0.34(4)	47.0	OSO	Y	Y
06105+1756	0.5(1)	7.7	2.2(2)	0.8(2)	0.2(2)	2.1	OSO	N	N
06114+1745	1.3(1)	7.4	3.0(1)	0.43(7)	0.25(6)	9.6	OSO	N	N
06117+1350	1.8(1)	18.2	4.6(1)	0.53(6)	0.26(4)	15.1	OSO	Y	N
06155+2319	0.8(1)	-5.6	2.4(1)	0.6(1)	0.0(1)	3.4	OSO	N	N
06308+0402	0.8(1)	15.8	2.3(2)	0.5(1)	0.2(1)	3.6	OSO	Y	Y
06319+0415	~ 1.4	13.9				10.8	OSO	N	Y
06380+0949	<0.3						OSO	N	N
06384+0932	4.4(1)	8.1	5.4(1)	0.51(4)	0.42(2)	54.6	OSO	Y	Y

^a H₂O masers according to Henning et al. 1992^b outflow according to Wu et al. 1996^c Paper I^d 1999 data

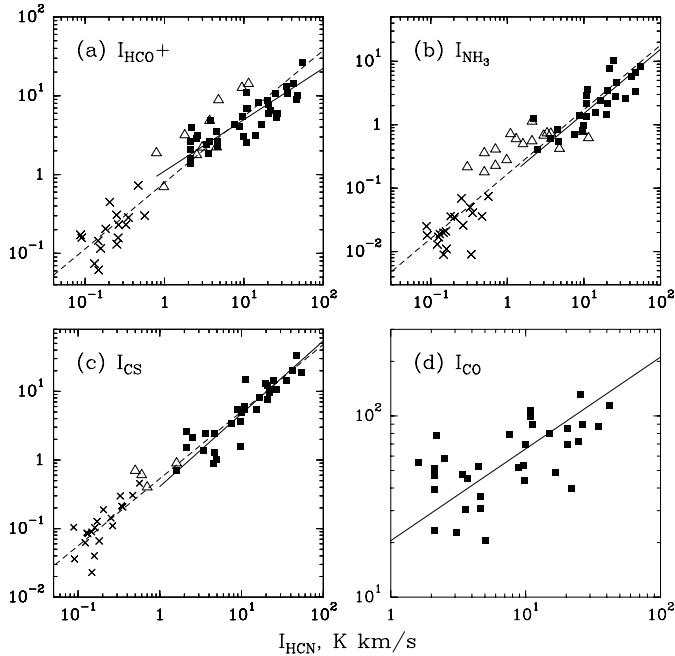


Fig. 2a–d. Integrated HCO^+ **a**, NH_3 **b**, CS **c** and CO **d** intensities versus HCN integrated intensities for the sample of bright FIR sources (filled squares), low-mass star-forming regions (open triangles), high-latitude cirrus and translucent cores (crosses). See text for the references

solid lines. The slopes of regression lines are close to ~ 1 for the $\log I(\text{CS})-\log I(\text{HCN})$ and the $\log I(\text{NH}_3)-\log I(\text{HCN})$ dependencies. The slopes are ~ 0.7 and ~ 0.5 for the $\log I(\text{HCO}^+)-\log I(\text{HCN})$ and $\log I(\text{CO})-\log I(\text{HCN})$ dependencies, respectively. The mean values of $I_{\text{mol}}/I(\text{HCN})$ ratios are 0.6 ± 0.4 , 0.5 ± 0.3 , 0.2 ± 0.1 and 10.2 ± 8.5 where I_{mol} means HCO^+ , CS, NH_3 and CO integrated intensities, respectively.

High correlations between integrated intensities of four molecular species which are considered to be high-density tracers (HCN , HCO^+ , NH_3 and CS) imply common line excitation mechanisms in the sample cores. Possible chemical, radiative transfer and optical depth source-to-source variations seem to be of minor importance. Lower correlation between CO and HCN integrated intensities could be due to the fact that the CO lines are more opaque and trace regions of lower density than the other lines under comparison.

In order to compare line parameters in high-mass star forming cores with those of low-mass star forming regions and cirrus cores we included in our analysis the data obtained in dark clouds, clouds associated with Herbig Ae/Be stars, Bok globules and high-latitude cirrus and translucent cores. The data were taken from Harju (1989), Scappini et al. (1994), Scappini & Codella (1996), Turner et al. (1997), Benson & Myers (1989), Turner (1995a, 1995b, 1996) and Zhou et al. (1989) and are also plotted in Fig. 2(a-c).

All the data sets including the sample of bright FIR sources cover ~ 3 orders of magnitude of integrated intensity range. High-mass, low-mass star-forming regions and cirrus cores concentrate in different regions of the diagrams (see Fig. 2(b,c)). Correlations found for bright FIR sources remain practically

unchanged with addition of the data for low-mass star-forming regions and high-latitude cirrus and translucent cores. Correlation coefficients are as high as 0.94–0.97 for the total data sets in Fig. 2(a-c) while regression lines (drawn by dashed lines) go very close to those obtained for the sample of bright FIR sources alone except for the $\log I(\text{HCO}^+)-\log I(\text{HCN})$ dependence that has slightly higher slope (~ 0.8) than of the dependence for the sample of bright FIR sources alone.

It is clear that common line excitation and molecular formation mechanisms of different high-density tracers should exist in high-mass, low-mass star forming regions and cirrus cores. It is doubtful, however, that radiative excitation could be effective in all these different types of cores. E.g., radiative excitation of CS and, probably, HCN via lowest vibrational states is important only in regions very close to IR sources (Carroll & Goldsmith 1981). Optical depth variations also cannot produce the observed correlations over such extended integrated intensity ranges because in this case the most intense lines in bright FIR sources should be highly saturated. Therefore, the most probable excitation mechanism for the considered molecules could be collisional excitation. Different densities as well as different molecular abundances and velocity dispersions in different types of cores seem to be important in producing the observed correlations.

There are kinetic temperature estimates for 16 sources from the sample derived from ammonia data (Schreyer et al. 1996, Zinchenko et al. 1997) which are $\sim 15 - 30$ K. However, no significant correlation is found between $J = 1 - 0$ HCN parameters and kinetic temperatures. R_{12} ratios decrease from ~ 0.6 to ~ 0.4 as kinetic temperature increases, yet, the significance of this correlation is not high due to the small number of data points.

4.2. Line width comparison

In Fig. 3 we compare HCN line widths with those of other molecular species for the sources where line widths are determined. All molecular line widths correlate with those of HCN with correlation coefficients of ~ 0.7 for HCO^+ and CS versus HCN (Fig. 3 (a) and (c), respectively) and of ~ 0.5 for NH_3 and CO versus HCN line widths (Fig. 3 (b) and (d), respectively). The lines shown in Fig. 3 correspond to $\Delta V_{\text{mol}} = \Delta V_{\text{HCN}}$ where ΔV_{mol} means HCO^+ , NH_3 , CS or CO line widths. The CO line widths are higher than those of HCN, while the ammonia widths are lower than HCN. The HCO^+ and HCN line widths for the sample sources are close to each other; both have the same mean value 3.1(0.8). The mean values of CS, NH_3 and CO line widths are 3.0(0.9), 2.2(0.5) and 4.3(1.3), respectively.

All molecular line widths are much higher than probable thermal widths calculated from kinetic temperatures ($< 0.2 \text{ km s}^{-1}$), reflecting either high optical depths or contributions from non-thermal motions. However, at that angular resolution very high optical depths seem to be unreal for the lines of high density tracers, because peak line intensities are much smaller than possible kinetic temperatures. The HCN profiles also do not show any evidences of saturation such as flat tops or

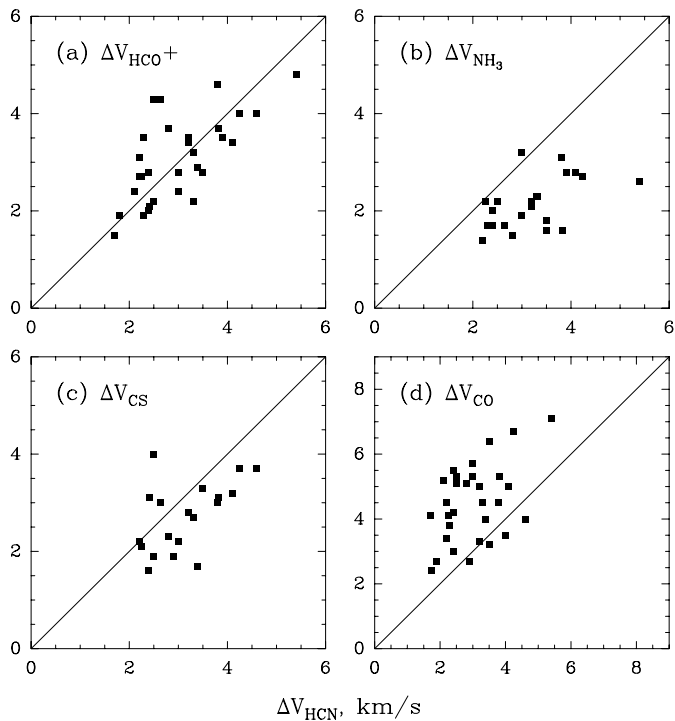


Fig. 3a–d. HCO^+ **a**, NH_3 **b**, CS **c** and CO **d** line widths versus HCN line widths. $\Delta V_{\text{mol}} = \Delta V_{\text{HCN}}$ lines are also shown

self-reversals for the sources compared. The differences in line widths of different species could therefore reflect differences in velocity dispersions of non-thermal motions which could in turn attribute to different sizes of emission regions within the same beam. In such a case NH_3 should be more centrally condensed on the line of sight than other species under comparison while HCO^+ and HCN should have more flatter distributions than NH_3 .

5. Comparison between HCN data and parameters of IRAS sources

Comparison between parameters of IRAS sources and molecular lines is widely considered to give a clue to how dust and gas are coupled in dense molecular cloud cores. Correlations revealed by Wouterloot et al. (1988) between kinetic temperatures of ammonia cores, line widths and IRAS point source luminosities showed that stellar objects embedded into molecular cloud cores play an essential role in heating and dynamical support of these cores. However, further investigations do not always confirm these trends. E.g., there are no correlations found between ammonia line parameters and IRAS point source luminosities for the sources of our sample (Schreyer et al. 1996) despite the distribution of data over the same range as the data from Wouterloot et al. (1988).

Carpenter et al. (1990) have calculated FIR luminosities for 18 sources of the present sample from IRAS images at $60 \mu\text{m}$ and $100 \mu\text{m}$ for the regions they mapped in CO. We compared CO and FIR luminosities from Carpenter et al. (1990) and found a prominent correlation with correlation coefficient 0.75. The

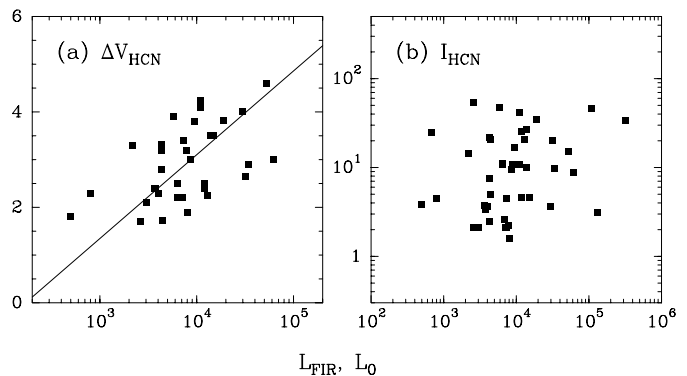


Fig. 4a and b. HCN line widths **a** and HCN integrated intensities **b** versus luminosities of IRAS sources. Least-squares fit is also shown

CS luminosities calculated for 16 objects observed by Carpenter et al. (1993) also show a correlation with FIR luminosities with the same correlation coefficient.

We compared HCN line parameters with IRAS point source luminosities (L_{FIR}) which lie in the range $\sim 4 \cdot 10^2 - 3 \cdot 10^5 L_{\odot}$ (Schreyer et al. 1996). We found no correlations between $F = 2 - 1$ main beam temperatures, R_{12} and R_{02} ratios and L_{FIR} . There is a correlation between HCN line widths and L_{FIR} (Fig. 4a, correlation coefficient is ~ 0.5). 06384+0932 has been excluded from the comparison because the observed HCN line width in this source is probably the result of blending of two velocity components (Wouterloot et al. 1988). HCN integrated intensity does not correlate with L_{FIR} (Fig. 4b).

Dust color temperatures (Schreyer et al. 1996) are $\sim 25 - 40$ K and are systematically higher than gas kinetic temperatures. They show no correlation with HCN line parameters.

Weak or no correlations between HCN line parameters and parameters of IRAS point sources, probably, result from the fact that IRAS is not sensitive to most of the cold dust which in turn can be better mixed with dense gas traced by HCN. On the other hand, in order to search for possible correlations it could be more fruitful to compare gas and dust parameters both integrated over the same regions as it follows from comparison of the data taken from Carpenter et al. (1990, 1993) or to compare distance independent parameters.

In order to avoid possible uncertainties introduced by distances we also compared HCN integrated intensities with flux densities at $100 \mu\text{m}$ (S_{100}) and found a correlation with correlation coefficient of ~ 0.5 . A comparison between $I(\text{HCN})$ and IRAS luminosity divided by distance squared (L_{FIR}/D^2) shows similar correlation (correlation coefficient is ~ 0.5). Other HCN line parameters do not show significant correlations either with S_{100} or L_{FIR}/D^2 .

6. Statistical distributions of the sources with associated H_2O masers and high-velocity outflows

Columns 8 and 9 of Table 2 contain letter flags indicating if the source has associated water masers according to Henning et al. (1992) and/or high velocity molecular outflow according to Wu et al. (1996). H_2O masers and molecular outflows are

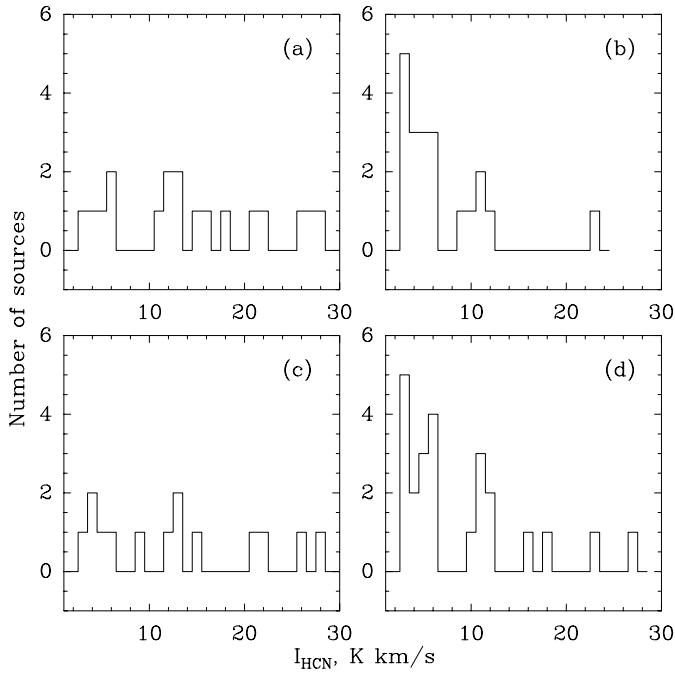


Fig. 5a–d. Number of the sources with **a** and without **b** associated H_2O masers and with **c** and without **d** molecular outflows versus HCN integrated intensities

indicative of high dynamic activity of young stellar objects. 24 sources of the sample have associated water masers (47%), 20 sources (39%) demonstrate molecular outflows and 17 of them have both associated water maser and molecular outflow. Seven sources with no HCN detections have both no associated H_2O masers and outflows.

The distributions of the sources with and without H_2O masers versus HCN integrated intensity are plotted in Fig. 5(a,b) while similar distributions for the sources with and without outflows are plotted in Fig. 5(c,d). The distributions of the sources without associated H_2O masers as well as without outflows are narrower and peak at lower $I(\text{HCN})$ values as compared with the distributions of the sources having associated H_2O masers and outflows. Similar distributions were found by Schreyer et al. (1996) for the sources with and without associated water masers versus NH_3 and HCO^+ integrated intensities. As a result, the sources with most intense HCN lines most probably have associated H_2O masers and demonstrate outflow activity while the lack of water maser emission implies weak or undetectable HCN emission.

7. $J = 1 - 0$ HCN hyperfine intensity ratios.

Modelling results

R_{12} hyperfine intensity ratios versus R_{02} are shown in Fig. 6; both have uncertainties < 0.1 . Corresponding error bars are indicated. The LTE $R_{12}(R_{02})$ dependence is also shown. All the data points concentrate in the lower left corner under the LTE curve demonstrating well-known anomalies of intensity ratios. The data points lie in the following ranges: $0.3 < R_{12} < 0.66$

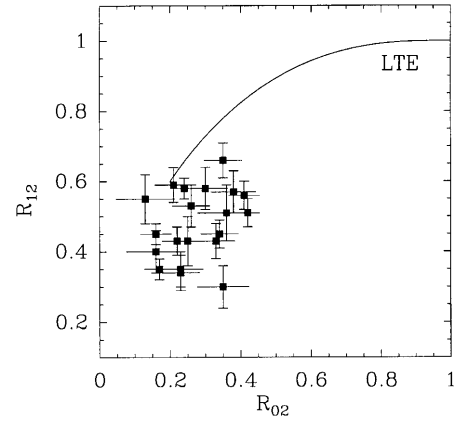


Fig. 6. R_{12} hyperfine intensity ratios versus R_{02} ratios both having uncertainties < 0.1

with the mean value $0.48(0.10)$ and $0.13 < R_{02} < 0.42$ with the mean value $0.28(0.09)$. There is no difference in R_{12} and R_{02} distributions for the sources with and without associated H_2O masers.

Note, that several sources with an intense $F = 2 - 1$ component demonstrate small deviations from a single HCN Gaussian. Those deviations which could be connected either with high-order baseline distortions or real emission features usually can be fitted by a second Gaussian triplet of higher width. We have excluded these sources from further analysis except 05480+2545 and 06056+2131 where the spectra show clearly resolved narrow components over pedestal emission. Deconvolution of these spectra into two Gaussian triplets reveals the following parameters of narrow components: $T_{\text{MB}} = 2.3(0.2)$ K, $R_{12} = 0.59(0.09)$, $R_{02} = 0.24(0.06)$ and $\Delta V = 2.6(0.1)$ km s^{-1} for 05480+2545 and $T_{\text{MB}} = 3.6(0.3)$ K, $R_{12} = 0.46(0.10)$, $R_{02} = 0.22(0.06)$ and $\Delta V = 3.2(0.1)$ km s^{-1} for 06056+2131. The sources with line widths higher than 4 km s^{-1} also have been excluded from the analysis because their $F = 2 - 1$ and $F = 1 - 1$ components are unresolved which can cause ambiguities in deriving correct values of intensity ratios. Three of the remaining 13 sources (05345+3157, 05480+2545, 06006+3015) have R_{12} and R_{02} close to the optically thin values (0.6 and 0.2, respectively). Eight sources (02575+6017, 03035+5819, 03064+5638, 05358+3543, 05375+3540, 06056+2131, 06063+2040, 06114+1745) demonstrate highly anomalous R_{12} and nearly optically thin R_{02} ratios: (0.34–0.46) and (0.16–0.25), respectively. Two other sources demonstrate enhanced R_{02} ratios: (0.3–0.35) and following R_{12} ratios: 0.3 for 04324+5106 and 0.58 for 05490+2658. $T_{\text{MB}}(F = 2 - 1)$ and ΔV for these 13 sources are: 0.65 K–5.5 K and 1.7 km s^{-1} – 3.5 km s^{-1} , respectively. R_{12} and R_{02} for these sources are plotted versus $\Delta V(\text{HCN})$ in Fig. 7(a) and (b), respectively. There are no correlations between R_{12} and R_{02} ratios and both intensities and widths of the main component. Five of the 13 selected sources were mapped by Carpenter et al. (1993) in the $J = 2 - 1$ CS line. Four of them (02575+6017, 04324+5106, 05375+3540, 06056+2131) have a centrally

peaked CS distribution and demonstrate $R_{12} = 0.3 - 0.48$ while the remaining one (05490+2658) with a fragmented CS distribution has $R_{12} = 0.58$.

Anomalies of the intensity ratios of the $J = 1 - 0$ HCN hyperfine components are a well-known phenomenon which depends on the gas temperature. Usually clouds with kinetic temperatures of ~ 10 K (dark clouds) demonstrate either nearly optically thin or enhanced R_{12} values (see e.g. Harju 1989, Sandell et al. 1983). On the other hand, in clouds with kinetic temperatures $\gtrsim 20$ K (warm clouds) R_{12} ratios are usually much lower than 0.6. These effects are well explained by population redistribution in overlapping thermally broadened hfs components in the HCN $J = 2 - 1$ transition which effectively differs for the clouds with kinetic temperatures of ~ 10 K and of $\gtrsim 20$ K (Gottlieb et al. 1975, Guilloteau & Baudry 1981, hereafter GB; Turner et al. 1997). According to GB, R_{12} and R_{02} ratios decrease below optically thin values (0.6 and 0.2, respectively) in warm clouds demonstrating prominent anomalies as long as overlapping components in the $J = 2 - 1$ transition become optically thick. While the standard approach includes only thermal line overlaps the observed HCN lines demonstrating anomalies have highly suprathermal line widths implying either additional local microturbulent broadening or some macro-turbulent or systematic motions on the line of sight. In order to explain the observed HCN spectra with anomalous component ratios and suprathermal line widths one needs to perform non-LTE model simulations to solve for nonlinear radiative transfer problems in the case of hyperfine splitting.

Preliminary HCN simulations performed for a homogeneous isothermal ($T_{\text{KIN}} = 20 - 50$ K) spherically-symmetric cloud model with constant excitation conditions throughout the cloud and purely thermal broadening (similar to GB model) show that the R_{12} and R_{02} anomalies occur within $\sim 10^{13} - 10^{15} \text{ cm}^{-2}$ column density range as far as number density is $\leq 10^7 \text{ cm}^{-3}$. As it was shown in Paper I, hyperfine intensity ratios are rather sensitive to velocity dispersion of local microturbulent motions (hereafter microturbulent velocity, V_{mt}) which gives an additional broadening due to local non-thermal motions. As microturbulent velocity increases the anomalies become less prominent and completely disappear at $V_{\text{mt}} \geq 2 \text{ km s}^{-1}$. This was also noted by Gottlieb et al. (1975). At higher microturbulent velocities model $R_{12}(R_{02})$ dependence goes asymptotically to the LTE curve. Thus, kinetic temperatures might have an effect on hyperfine intensity ratios only if local microturbulent velocity dispersions are about or lower than thermal ones while the observed line widths are much higher than thermal widths.

Although a homogeneous model with constant excitation conditions is rather simplified for detailed analysis of the HCN emission coming from the cores with bright FIR sources, it can give a correct qualitative description of how intensity ratios depend on microturbulent velocity. As it was shown in Paper I, this model with $T_{\text{KIN}} = 30$ K and number densities $10^4 - 10^6 \text{ cm}^{-3}$ fails to reproduce the observed R_{12} ratios and line widths for several sources of the sample. This result leads to the conclusion that these sources should have microturbulent velocity and density gradients along the line of sight to allow peak intensi-

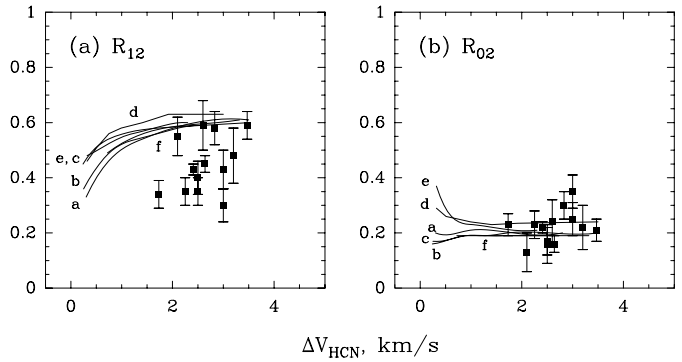


Fig. 7a and b. R_{12} **a** and R_{02} **b** hyperfine intensity ratios versus line widths. The curves correspond to the results of calculations for multi-zone microturbulent models. See text for details

ties of hfs components to come from inner core regions with nearly thermal broadening while line wings should come from outer regions. Alternatively, the cores could consist of small unresolved clumps having nearly thermal velocity dispersions while the observed line widths reflect velocity dispersions of interclump motions.

7.1. Microturbulent multi-zone model results

We performed model calculations for spherically-symmetric microturbulent multi-zone models where parameters (density, temperature and microturbulent velocity) can be power-law functions of radius. A model is similar to the one described by Turner et al. (1997) and uses Varshalovich & Khersonsky (1977) collisional rates. HCN abundances are assumed to be constant throughout the core. In order to compare the results of calculations with observational data the calculations were performed for HCN column densities $\gtrsim 3 \cdot 10^{12} \text{ cm}^{-2}$. At these $N(\text{HCN})$ model profiles often are self-reversed due to a decrease of excitation temperatures to the edge when lines become optically thick. For example, at 10^5 cm^{-3} and $V_{\text{mt}} = 0 \text{ km s}^{-1}$ the model spectra become self-reversed at $N(\text{HCN}) \gtrsim 10^{13} \text{ cm}^{-2}$. Self absorption occurs at lower values of $N(\text{HCN})$ if number density decreases outward but it can be shifted to higher $N(\text{HCN})$ values by choosing higher central densities or if microturbulent velocity increases outwards.

Because none of the considered profiles demonstrate self absorption, we restricted the model parameters to the values at which model profiles are close to Gaussian. It is found that nearly Gaussian $J = 1 - 0$ HCN model profiles with prominent anomalies ($R_{12} < 0.5$) exist within the following range of number densities: $3 \cdot 10^5 \text{ cm}^{-3} - 3 \cdot 10^6 \text{ cm}^{-3}$.

The curves (a-c) in Fig. 7(a,b) correspond to R_{12} and R_{02} values plotted versus line width for a 10-zone model with kinetic temperature of 30 K and densities: $3 \cdot 10^5 \text{ cm}^{-3}$ (a), 10^6 cm^{-3} (b) and $3 \cdot 10^6 \text{ cm}^{-3}$ (c). Microturbulent velocities increase from 0 km s^{-1} to 2 km s^{-1} along each curve. $N(\text{HCN})$ is $\approx 2 \cdot 10^{13} \text{ cm}^{-2}$. The $F = 2 - 1$ intensity decreases with line width from ~ 5 K down to ~ 1 K when line width is $> 1 \text{ km s}^{-1}$.

Higher column densities lead to higher $F = 2 - 1$ intensities with saturated or self-reversed profiles.

Three other curves correspond to the following models:

- $n \propto r^{-1}$ with central density 10^6 cm^{-3} , $T_{\text{KIN}} = 30 \text{ K}$ (d);
- $n = 10^6 \text{ cm}^{-3}$, $T_{\text{KIN}} \propto r^{-0.4}$ with 30 K at the center (e);
- $n = 10^6 \text{ cm}^{-3}$, $T_{\text{KIN}} = 30 \text{ K}$ and $V_{\text{mt}} \propto r^{0.5}$ (f).

It is clear from Fig. 7(a) that R_{12} anomalies occur only at $\Delta V \lesssim 1 \text{ km s}^{-1}$ confirming the thermal nature of the effect while the observed data points correspond to higher line widths. R_{02} ratios are practically insensitive to the model being close to 0.2 except model (e) which gives higher values at $\Delta V \lesssim 1 \text{ km s}^{-1}$. The effect of self absorption can be reduced by increasing power-law index of $V_{\text{mt}}(r)$ dependence. However, as soon as a power-law index becomes higher than 0.5, the model line profiles become prominently non-Gaussian with a sharp peak and extended wings.

Thus, it seems unlikely that the microturbulent model with a smooth distribution of parameters can reproduce the observed HCN profiles with prominent R_{12} ratio anomalies and high line widths.

7.2. Clumpy model results

There are many indications that molecular clouds and their cores are clumpy on all spatial scales down to telescope resolution limits (see Goldsmith 1995). This is implied by nearly identical line widths and map sizes of different molecules with different critical densities as well as by nearly constant volume densities derived from multitransitional analysis in clouds with strong column density variations. One more reason for clumpiness comes from a correlation detected between C I and C II emission maps and molecular maps (for clouds with external sources of ionization). The early ideas about the possibility of clumpy structure came from analysis of molecular line profiles most of which have highly suprathermal line widths without any evidence of self-reversals and saturation which can be explained as a superposition of emission from a large number of individual unresolved clumps within the telescope beam. Recent multi-transitional CS and C^{34}S modelling (Juvela 1998) has shown that clumpy models can be fruitful for analysis of molecular line maps toward regions of high-mass star formation. Juvela (1998) as well as Park & Hong (1998) show that a use of clumpy models can help to avoid problems related to the line profile self absorption in microturbulent models. If the clump's volume filling factor is sufficiently small, the emission from a single clump can escape from the cloud without significant scattering thus providing information about its parameters. Observed line widths in this case should reflect velocities of interclump motions. One might expect that the anomalies of the $J = 1 - 0$ HCN hyperfine structure that originate in clumps with nearly thermal local line widths can be seen in emergent profiles within such models.

We developed a program that calculates HCN excitation parameters as well as emergent $J = 1 - 0$ HCN profiles within a spherically-symmetric model that can consist of many clumps unresolved by a telescope beam. Clumps are considered to be

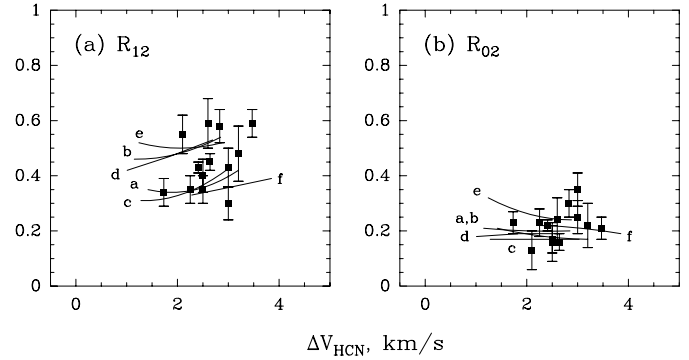


Fig. 8a and b. R_{12} **a** and R_{02} **b** hyperfine intensity ratios versus line widths. The curves correspond to the results of clumpy model calculations. See text for details

homogeneous isothermal balls of the same size without internal structure. Physical parameters of each clump (number density, kinetic temperature, microturbulent velocity) as well as velocity dispersion of interclump motions can be represented as functions of distance from the center. The HCN excitation parameters are calculated for one representative clump in each zone by an iterative method. A detailed model description is given in the Appendix.

First we used a model that is divided into 10 equally spaced concentric zones each of which contained randomly distributed clumps. A single clump's diameter was set equal to 1/5 of the zone width. No additional microturbulent broadening was assumed. The model parameters were: clump number density, velocity dispersion of interclump motions, which determined the resulting line width, HCN abundance and kinetic temperature of clumps. In order to reduce statistical fluctuations (ripples) on emergent profiles the resulting HCN $J = 1 - 0$ spectra were averaged over 100 independent lines of sight. The volume filling factor of clumps was constant throughout the model cloud having the value of 0.2. Model spectra were fitted by Gaussian triplets in order to compare line parameters with the observed values.

Consistent with the results of Juvela (1998) and Park & Hong (1998) it was found that clumpiness helps to avoid line profile self absorption both due to effects of macro turbulence and spatial dilution.

In Fig. 8(a,b) we plotted the observed R_{12} and R_{02} intensity ratios, respectively, versus line widths along with model curves. Clump number density is either constant: $3 \cdot 10^4 \text{ cm}^{-3}$ (a), 10^5 cm^{-3} (b,c), $3 \cdot 10^5 \text{ cm}^{-3}$ (d) or decreases outwards as $n \propto 3 \cdot 10^5 \cdot r^{-1}$ (e,f). The velocity dispersion of interclump motions increases from 0.5 km s^{-1} to 2 km s^{-1} or from 1 km s^{-1} to 2 km s^{-1} (f) because of self-absorption on line profiles at smaller velocities in the latter case. $N(\text{HCN})$ is $\approx 10^{14} \text{ cm}^{-2}$ (a,c,f) and $\approx 3.5 \cdot 10^{13} \text{ cm}^{-2}$ (b,d,e). Kinetic temperature has a constant value of 30 K (a-d) or decreases outwards as $T_{\text{KIN}} \propto 30 \cdot r^{-0.4}$ (e,f). The $T(F = 2 - 1)$ temperature decreases along each curve with increasing line width being in the range of the observed intensities of the sources under comparison. Higher column densities lead to smaller R_{12} and vice versa. Lower number densities

lead to flat-topped and self-reversed line profiles while higher number densities lead to higher $F = 2 - 1$ intensities out of the observed range.

It is clear from Fig. 8 that the HCN spectra observed in 8 sources with reduced R_{12} ratios (~ 0.4) and nearly optically thin R_{02} values (~ 0.2) can be reproduced, e.g., with clump number density $\sim 10^5 \text{ cm}^{-3}$ and $N(\text{HCN}) \approx 10^{14} \text{ cm}^{-2}$ (curve c). R_{02} values are not so critical to number and column densities but they are sensitive to the value of kinetic temperature being higher when T_{KIN} decreases outwards (curve (e)). It is difficult to explain within the considered range of model parameters the enhanced R_{02} values (~ 0.3) observed in 04324+5106 and 05490+2658 where ΔV are higher than 2.5 km s^{-1} . For reproducing these anomalies one, probably, needs to include an extended diffuse envelope into the model which could effectively absorb $F = 2 - 1$ component intensity relative to $F = 0 - 1$.

As the next step, we examined the clumpy model more thoroughly by fitting model profiles to the HCN and H^{13}CN spectra observed toward the bright infrared source S140 IRS1. Though not included in the considered sample, this well-known high-mass star-forming region demonstrates very strong HCN lines with the same kind of anomaly that has been detected in the 8 sources of our sample. Moreover, S140 IRS1 has been widely observed and modelled in various lines that gives a possibility to compare with the parameters found by other authors. The results of our model simulations are given in the next section.

7.3. L1204/S140 IRS1 dense core – implications for clumpy structure

The dense core of the L1204 molecular cloud is located northeast of the S140 optical H II region and contains a cluster of three infrared sources, IRS 1–3, which are identified with high-mass stars of spectral type B (Evans et al. 1989). The multitransitional CS observations of the core (Zhou et al. 1994) reveal two different components on a subarcminute spatial scale: a spherical one centered on IRS 1 which dominates in high- J CS emission and an arc component that dominates in low- J CS emission and NH_3 emission (Zhou et al. 1993) being closer to the photon-dominated interface region between the H II region and molecular cloud. The arc component demonstrates resolved clumpy structure (Hayashi & Murata, 1992) while the spherical component shows a central disk surrounded by a cavity embedded in an inhomogeneous dense envelope (Wilner & Welch 1994, Minchin et al. 1993, Harker et al. 1997). The core also contains a bipolar outflow that originates at IRS 1 (Bally & Lada 1983, Hasegawa et al. 1991).

The $J = 1 - 0$ HCN observations toward S140 IRS1 performed at RT-22 (Pirogov et al. 1995) as well as at OSO during our observing session in February 1996 reveal a narrow spectral component blended with a high-velocity component of lower intensity. The Gaussian fitting by two HCN triplets with different widths gave the following parameters for the stronger and narrower component: $T_{\text{MB}}(F = 2 - 1) = 10 \text{ K}$, $\Delta V = 2.6 \text{ km s}^{-1}$ and $R_{12} = 0.37$, $R_{02} = 0.24$. The anomaly of the $J = 1 - 0$ HCN spectrum is of the same kind as detected in 8 sources of the

present sample. The $J = 1 - 0 \text{ H}^{13}\text{CN}$ line parameters observed toward S140 IRS1 are the following: $T_{\text{MB}}(F = 2 - 1) = 1.2 \text{ K}$, $\Delta V = 2.2 \text{ km s}^{-1}$ and $R_{12} \approx 0.6$, $R_{02} \approx 0.2$ (Pirogov et al. 1995). The ratios of hyperfine intensity components imply that the H^{13}CN line is optically thin. The lower limit of the H^{13}CN column density ($N(\text{H}^{13}\text{CN})$) calculated under the LTE assumption ($T_{\text{ex}} = 10 \text{ K}$) is $\gtrsim 8 \cdot 10^{12} \text{ cm}^{-2}$ (Pirogov et al. 1995). Our observations with $40''$ toward IRS 1 covered most of the spherical component and, probably, a part of the arc component.

In order to reproduce the observed $J = 1 - 0$ HCN and H^{13}CN spectra toward S140 IRS1 we performed detailed model calculations of the spherical component. We took 0.44 pc for the outer radius (Zhou et al. 1994) and divided the model core into 17 zones, each zone having 0.026 pc width. Clump parameters: number density, kinetic temperature as well as volume filling factor and velocity dispersion of interclump motions were kept constant within each zone and could be varied from zone to zone as power-law functions of a zone's radius. Microturbulent velocity was set to zero in order to obtain the effect of thermal line overlaps alone. The velocity dispersion of interclump motions was set to 1.3 km s^{-1} according to the optically thin H^{13}CN line width. Following Zhou et al. (1994) we assumed the central zone to be empty in order to account for the cavity around IR sources. Clumps have constant size throughout the model core. The HCN abundance was assumed constant and its value was varied in order to fit the calculated $F = 2 - 1$ intensity to the observed value.

The resulting spectrum was calculated by averaging spectra for all independent lines of sight within the projection of each zone on the plane of the sky and then convolving the averaged model spectra corresponding to different projections with a $40''$ beam. The quality of fitting was controlled by the sum of squares of residuals (χ^2) between model and observed values of line profile temperatures.

A clump's number density and volume filling factor were set to be power-law functions of radius: $n = n_0(r/R)^{-\alpha}$ and $P = P_0(r/R)^{-\beta}$, respectively, where n_0 and P_0 correspond to the second zone and R is the outer radius. While searching for suppressed R_{12} ratios together with $R_{02} \approx 0.2$ or slightly higher we found that the best fits occur at kinetic temperatures $\lesssim 20 \text{ K}$. This could be related to the fact that the overlaps of the second pair of closely located components in the $J = 2 - 1$ transition ($F = 2 - 2$ and $F = 1 - 0$, see GB) which lead to suppressed R_{02} ratio are still effective at temperatures higher than 20 K . We set the kinetic temperature to have the following law: $T_{\text{KIN}} = 30(r/R)^{-0.4}$ which gives 30 K in the second zone and 10 K at the edge of the cloud. The best fit parameters ($\chi^2 = 9.3$) correspond to $n_0 = 1.8 \cdot 10^6 \text{ cm}^{-3}$, $\alpha = 0.6$, $P_0 = 0.2$ and $\beta = 0.3$. Microturbulent CS modelling performed by Zhou et al. (1994) resulted in the following radial dependence of number density: $n = 1.4 \cdot 10^6(r/R)^{-0.8}$ which has a power-law index close to the total $n(r)$ and $P(r)$ index from our results. Lower kinetic temperatures (e.g. 13 K for all zones) can give even better fits, yet, low temperatures contradict with high HCO^+ line intensities observed toward S140 IRS1 with $20''$ resolution (Hasegawa et al. 1991). The number of clumps within the first 4

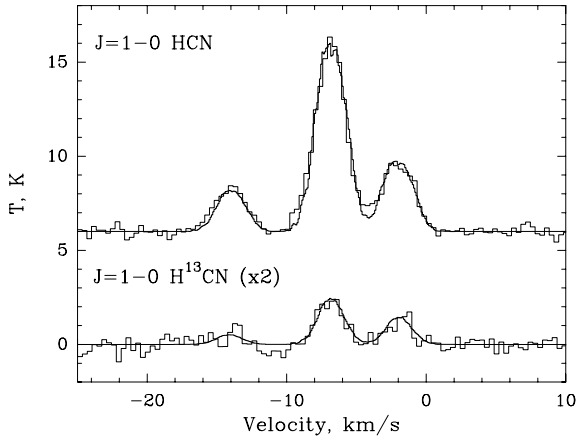


Fig. 9. The $J = 1 - 0$ HCN and H^{13}CN profiles toward S140 IRS1 (Pirogov et al. 1995). Smooth curves correspond to the modelling results within the clumpy model. See text for details

zones which give the main contribution to the resulting spectrum is ~ 16000 with an average volume filling factor of 0.11 which is somewhat lower than estimates made by other authors (Zhou et al. 1994, Spaans & Dishoeck 1997). The HCN abundance is $\sim 5 \cdot 10^{-9}$.

Because H^{13}CN lines are optically thin and the R_{12} and R_{02} ratios are approximately equal to 0.6 and 0.2, respectively, being insensitive to particular forms of density and volume filling factor laws, it is much easier to get the best fit in this case. We used the power-law parameters from the HCN fitting and fit only the $F = 2 - 1$ peak intensity varying the abundance and allowing $N(\text{H}^{13}\text{CN})$ to be not lower than the LTE value. The best H^{13}CN fit ($\chi^2 \approx 3.3$) was found at $X(\text{H}^{13}\text{CN}) \approx 1.8 \cdot 10^{-10}$. The HCN and H^{13}CN spectra are shown in Fig. 9 together with the best fitting curves.

Among the observed parameters of the HCN and H^{13}CN lines, the most uncertain are line intensities while hyperfine intensity ratios and line widths seem to be better determined parameters. This is due both to calibration uncertainties and uncertainties introduced by conversion of antenna temperatures into brightness temperatures. Allowing for $\sim 20\%$ uncertainties of line intensities leads to $\geq 50\%$ uncertainties for calculated HCN and H^{13}CN abundances.

8. Conclusions

We presented the results of the $J = 1 - 0$ HCN observations toward 34 galactic star-forming regions associated with bright FIR sources ($S(100 \mu\text{m}) > 500 \text{ Jy}$). Together with 17 sources observed in this line earlier (Pirogov et al. 1996) they form a complete sample of bright IRAS sources located in the outer Galaxy ($0^h < \alpha < 12^h$; $\delta > 0^\circ$). The sample sources are associated with high-mass young stellar objects embedded in dense molecular cloud cores.

The goal of this investigation was to search for HCN emission toward dense cores associated with bright FIR sources. We studied their physical properties by comparing HCN line parameters with parameters of other molecular lines taken from

literature as well as with parameters of the IRAS sources. We also tried to select the most adequate model of HCN emission.

HCN emission has been detected in 44 sources of 51 (86%). HCN column densities are $\gtrsim 3 \cdot 10^{12} \text{ cm}^{-2}$ for the sources where HCN was detected.

The comparison of the HCN integrated intensities with those of HCO^+ , NH_3 , CS and CO taken from literature reveal strong correlations with similar slopes of ~ 1 between line integrated intensities of the molecules known to be high density tracers (HCN, HCO^+ , NH_3 and CS). In order to enlarge the range of compared parameters we combined the data for bright FIR sources with molecular line data for dark clouds, small globules and cirrus cores. The correlations become higher with nearly the same slopes implying similar excitation and formation mechanisms of the molecules that trace high density gas in low-mass and high-mass star forming regions and cirrus cores. Collisional excitation of the considered molecules in regions with different densities as well as different molecular abundances and velocity dispersions in different types of cores seem to be important in producing these correlations. The following relations hold on the average over ~ 3 orders of magnitude of integrated intensities: $I(\text{HCN}) \gtrsim I(\text{HCO}^+) \sim I(\text{CS}) > I(\text{NH}_3)$ with ammonia integrated intensities being several times lower than HCN ones. Correlations are also found between CO and HCN integrated intensities as well as between HCN line widths and line widths of different molecular species for the present sample of bright FIR sources. The HCN lines have the same widths as the HCO^+ ones and higher widths than CS and, especially, NH_3 lines.

Weak correlations are found between HCN line widths and luminosities of IRAS sources as well as between HCN integrated intensities, IRAS flux densities at $100 \mu\text{m}$ and luminosities of IRAS sources divided by distance squared.

24 sources of the sample have associated water masers (47%) and 20 sources demonstrate outflow activity (39%). The sources with most intense HCN lines have associated water masers and molecular outflows while the lack of associated masers or outflows points to weak or no HCN emission.

In order to reproduce the anomalies of the $J = 1 - 0$ HCN hyperfine structure ($R_{12} < 0.6$) observed in several sources together with suprathermal HCN line widths model calculations are performed. Two spherical-symmetric models have been considered: a microturbulent one with a smooth density distribution and a clumpy model. It is found that in the parameter space explored the clumpy model is preferable in comparison with the microturbulent one due to the lack of self-reversals on calculated profiles and a possibility to obtain anomalous HCN hyperfine intensity ratios and suprathermal line widths.

Detailed clumpy model calculations have been performed to fit the observed HCN and H^{13}CN spectra toward the bright infrared source S140 IRS1. Power-law distributions of a clump's number density, $n_0 \propto r^{-\alpha}$, and volume filling factor, $P_0 \propto r^{-\beta}$, gave a best fit at: $n_0 = 1.8 \cdot 10^6 \text{ cm}^{-3}$, $\alpha = 0.6$, $P_0 = 0.2$ and $\beta = 0.3$. The number of clumps in a $40''$ beam should be ~ 16000 . The velocity dispersion of interclump motions is 1.3 km s^{-1} . Kinetic temperature of clumps should not exceed

30 K which is necessary to obtain $R_{02} \gtrsim 0.2$ together with $R_{12} \lesssim 0.4$ values observed in this source.

Acknowledgements. I am grateful to Dr. I. Zinchenko for the assistance during OSO observations, critical reading of the manuscript and helpful discussions. I would like to thank Dr. J.M. Carpenter for providing the $J = 2 - 1$ CS data tables for the bright FIR sources he observed and Dr. M. Juvela for providing his CS clumpy modelling results. I am also grateful to the referee, Dr. E. Churchwell, for many important comments and grammar corrections. I want to thank the staff of Onsala Space Observatory for technical support and especially Dr. L.E.B. Johansson for the help and hospitality. The work was supported by the INTAS grant 93-2168-ext and the Russian Foundation for Basic Research grant 96-02-16472.

Appendix A: a clumpy cloud model

Our clumpy model utilizes a multi-zone radiative transfer code developed earlier for a spherically-symmetric cloud with a smooth density distribution (Turner et al. 1997). It explores an ordinary iterative method instead of Monte Carlo method.

Model cloud consists of a set of concentric zones with the same width. Each zone is divided into cells with diameter lower or equal to a zone's width. Cells can be filled with a gas or be empty according to an integer random number generator which gives 1 with probability P (clump) or 0 (empty cell) with probability $(1-P)$. The probability P has the same statistical meaning as a clump's volume filling factor. Clumps are assumed to be isothermal and homogeneous without internal structure moving randomly with Gaussian velocity law. Individual clump's parameters (kinetic temperature, density and microturbulent velocity), as well as volume filling factor and velocity dispersion of interclump motions are constant within a zone and can be varied from zone to zone. Systematic velocities also can be taken into account.

HCN excitation is computed for one representative clump per zone. All other clumps in a zone are assumed to be identical to a given clump. Clump's line profile is assumed to be Gaussian with both thermal and microturbulent contributions to its width. The radiative transfer is solved by treating local overlaps of the hfs components according to the formulation of GB. An external radiation includes radiation coming from distant clumps and cosmic background radiation. Mean radiation field which enters into balance equations for level populations is calculated by angular and frequency integration of intensity weighted by normalized line profile function. Angular integration is calculated by summing radiation that comes to the clump along a number of rays separated by a fixed angular step. A radiation along particular ray summarizes contributions from distant clumps crossed by this ray. Projections of random and systematic velocity components on a given ray give particular Doppler shifts for emission coming from a distant clump. Spatial distribution of clumps is kept fixed only during calculation of HCN excitation for a given clump in a zone. Because all clumps in a zone are identical, next representative clump can take an arbitrary place in next zone. Therefore, it is possible to consider a new spatial distribution of clumps as all possible clumps configurations are statistically equivalent (see Pagani 1998).

Iteration process is similar to the one described by Turner et al. (1997). It includes a double-iteration scheme according to which HCN level populations are calculated for one clump per zone keeping populations in other clumps unchanged. After reaching an outer zone, resultant populations are compared with populations stored from previous iteration and if a relative difference is higher than the tolerance value (0.001) populations from last iteration are stored and the process repeats starting from the first (innermost) zone. After the iteration process converges, emergent line profiles are calculated for all independent lines of sights separated by angular size of a single clump. To reduce statistical fluctuations, resultant profiles are averaged over independent lines of sight within projection of each zone on a plane of a sky. These profiles can be convolved with a telescope beam to be compared with real spectra.

The negative features of the model are: a simplified representation of clumps as structureless balls, an absence of interclump gas, impossibility of considering more complex cloud geometries than spherically-symmetric. The positives of the model are: quick convergence, small amount of required memory and CPU time which make it possible to run on a common personal computer.

Similar approach is used for CS and HCO⁺ modelling.

References

- Anglada G., Estalella R., Pastor J., Rodriguez L.F., Haschick A.D., 1996, *ApJ* 463, 205
 Bally J., Lada C.J., 1983, *ApJ* 265, 824
 Benson P.J., Myers P.C., 1989, *ApJS* 71, 89
 Brand J., Blitz L., 1993, *A&A* 275, 67
 Bronfman L., Nyman L.-Å., May J., 1996, *A&AS* 115, 81
 Burov A.B., Vdovin V.F., Zinchenko I.I., et al., 1988, *PAZh* 14, 492 (*SvA Lett.* 14, 209)
 Carroll T.J., Goldsmith P.F., 1981, *ApJ* 245, 891
 Carpenter J.M., Snell R.L., Schloerb F.P., 1990, *ApJ* 362, 147
 Carpenter J.M., Snell R.L., Schloerb F.P., Skrutskie M.F., 1993, *ApJ* 407, 657
 Evans N.J. II, Mundy L.G., Kutner M.L., DePoy D.L., 1989, *ApJ* 346, 212
 Goldsmith P.F., 1995, In: Chiao R.Y. (ed.) *C.H. Townes Festschrift*. AIP
 Gottlieb C.A., Lada C.J., Gottlieb E.W., Lilley A.E., Litvak M.M., 1975, *ApJ* 202, 655
 Guilloteau S., Baudry A., 1981, *A&A* 97, 213 (GB)
 Harju J., 1989, *A&A* 219, 293
 Harker D., Bregman J., Tielens A.G.G.M., Temi P., Rank D., 1997, *A&A* 324, 629
 Hasegawa T.I., Mitchell G.F., Henriksen R.N., 1991, *AJ* 102, 666
 Hayashi M., Murata Y., 1992, *PASJ* 44, 391
 Henning T., Cesaroni R., Walmsley M., Pfau W., 1992, *A&AS* 93, 525
 IRAS Catalogs, 1988, *Infrared Astronomical Satellite (IRAS) Catalogs and Atlases*, NASA, RP-1190
 Juvela M., 1998, *A&A* 329, 659
 Lada C.J., 1985, *ARA&A* 23, 267
 Minchin N.R., White G.J., Padman R., 1993, *A&A* 277, 595
 Pagani L., 1998, *A&A* 333, 269
 Park Y.-S., Hong S.S., 1998, *ApJ* 494, 605

- Pirogov L., Lapinov A., Zinchenko I., Shul'ga V., 1996, A&A Transactions 11, 287 (Paper I)
- Pirogov L., Zinchenko I., Lapinov A., Shul'ga V., Myshenko V., 1995, A&AS 109, 333
- Plume R., Jaffe D.T., Evans N.J. II, 1992, ApJS 78, 505
- Plume R., Jaffe D.T., Evans N.J. II, Martin-Pintado J., Gomez-Gonzalez J., 1997, ApJ 476, 730
- Sandell G., Höglund B., Kislyakov A.G., 1983, A&A 118, 306
- Scappini F., Palumbo G.G.C., Bruni G., Bergman P., 1994, ApJ 427, 259
- Scappini F., Codella C., 1996, MNRAS 282, 587
- Schreyer K., Henning Th., Kömpe C., Harjupää P., 1996, A&A 306, 267
- Snell R.L., Huang Y.-L., Dickman R.L., Clausen M.J., 1988, ApJ 325, 853
- Snell R.L., Dickman R.L., Huang Y.-L., 1990, ApJ 352, 139
- Spaans M., van Dishoeck E.F., 1997, A&A 323, 953
- Turner B.E., 1995a, ApJ 444, 708
- Turner B.E., 1995b, ApJ 449, 635
- Turner B.E., 1996, ApJ 461, 246
- Turner B.E., Pirogov L., Minh Y.C., 1997, ApJ 483, 235
- Varshalovich D.A., Khersonsky V.K., 1977, Astrophys. Lett. 18, 167
- Wilner D.J., Welch W.J., 1994, ApJ 427, 898
- Wood D.O.S., Churchwell E., 1989, ApJ 340, 265
- Wouterloot J.G.A., Walmsley C.M., Henkel C., 1988, A&A 203, 367
- Wu Y., Huang M., He J., 1996, A&AS 115, 283
- Yang J., Umemoto T., Iwata T., Fukui Y., 1991, ApJ 373, 137
- Zhou S., Wu Y., Evans N.J. II, Fuller G.A., Myers P.C., 1989, ApJ 346, 168
- Zhou S., Evans N.J. II, Mundy L.G., Kutner M.L., 1993, ApJ 417, 613
- Zhou S., Butner H.M., Evans N.J. II, et al., 1994, ApJ 428, 219
- Zinchenko I., Mattila K., Toriseva M., 1995, A&AS 111, 95
- Zinchenko I., Henning T., Schreyer K., 1997, A&AS 124, 385
- Zinchenko I., Pirogov L., Toriseva M., 1998, A&AS 133, 337